An integral calculation method for incompressible three-dimensional boundary layers in axisymmetric diffusers

F. T. F. Morgado
Maintenance and Engineering Department, TAP—Air Portugal, Lisbon, Portugal

L. M. C. Gato
Department of Mechanical Engineering, Instituto Superior Técnico,
Technical University of Lisbon, Portugal

A direct integral method is presented for the calculation of incompressible turbulent three-dimensional boundary layers in axisymmetric walls. An inviscid throughflow program was combined with the boundary-layer calculation method to predict swirling flows in annular diffusers. Comparison between theoretical and experimental results indicates that predictions can be made in a great variety of boundary-layer flows with interest in turbomachinery. A design criterion based on boundary-layer development was used to compute the wall shape of axisymmetric diffusers.

Keywords: fluid flow; diffuser; boundary layer

Introduction

The purpose of a diffuser is to decelerate the flow and convert kinetic energy into pressure. The main parameters to be considered in its design are cross-sectional geometry; shape and size of boundary layers and main flow direction at inlet cross section; length; wall shape; and inlet-to-outlet cross-sectional area ratio. The design of a diffuser is conditioned primarily by boundary-layer separation. Experimental data show that maximum pressure recovery is attained with incipient stall at exit.[1-3] Care must be taken to avoid large detached regions that would reduce the diffuser effectiveness, creating unsteadiness and asymmetries. Hence, an accurate boundary-layer prediction method is required in the design of efficient diffusers.

The prediction of flows without swirl in axisymmetric diffusers has been the object of theoretical investigations using direct[4,5] and inverse[2,6] methods. These methods employ two-dimensional (2-D) boundary-layer calculations combined with inviscid throughflow methods. The presence of swirl in the external flow produces three-dimensional (3-D) boundary layers like the end-wall boundary layers encountered normally in turbomachinery.[7-10]

This article presents a direct integral method for the calculation of incompressible turbulent 3-D swirling boundary layers in axisymmetric walls. This method is an extension to three dimensions of the integral methods developed for 2-D boundary-layer calculation. An orthogonal coordinate system is defined in the meridian plane, and the following four differential equations are solved: (1) the tangential and meridional momentum integral equations; (2) an equation for the wall shear stress; and (3) an entrainment equation. The boundary-layer calculation needs, as input, the values of velocity and direction of the external flow. These are computed by an inviscid throughflow program based on the streamline curvature method.[11-13] An iterative procedure is used to displace the annular walls to account for the boundary-layers blockage effect. A design criterion based on the boundary-layer development is then considered in order to allow the computation of the walls shape of axisymmetric diffusers. The accuracy of the boundary-layer calculation method is assessed by applying it to some test cases for which a sufficiently complete set of experimental data could be found in the literature.

Address reprint requests to Professor Gato at the Department of Mechanical Engineering, Instituto Superior Técnico, Technical University of Lisbon, 1096 Lisbon Codex, Portugal.

Received 27 July 1989; accepted 9 October 1990

The boundary-layer method

The deflection of a rotational flow produces the development of the streamwise component of vorticity, and this generates the secondary flow. This type of flow is particularly important in turbomachinery, where the boundary layers that grow on the casing and hub walls are deflected by the stationary and rotating blades. Figure 1 shows a typical 3-D boundary-layer velocity profile. Superposed on the main flow is a secondary flow in a direction normal to the free stream. At the wall the flow obeys the nonslip condition.

We consider an orthogonal coordinate system (m, θ, n), where m is measured along the projection on the meridian plane of the external streamline at the edge of the boundary layer, n is measured along the direction normal to m on the same plane, and θ is the circumferential angular coordinate (Figure 2). We consider the flow to be axisymmetric and assume the boundary-layer thickness δ to be always small in comparison with the radius R of the wall surfaces. If we further consider the usual boundary-layer assumptions and perform the integration of the m and θ-momentum equations with respect to the direction normal to the wall, we obtain[14]

the m-momentum integral equation

$$\frac{d\theta_{mm}}{dm}+\frac{1}{C_m}\frac{dC_m}{dm}(2\theta_{mm}+\delta_m^*)+\left(\frac{\sin\lambda}{R}+K_n\right)\theta_{mm}$$

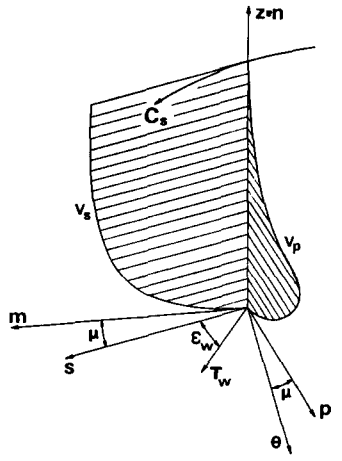

Figure 1 Streamwise and cross-flow velocity profiles

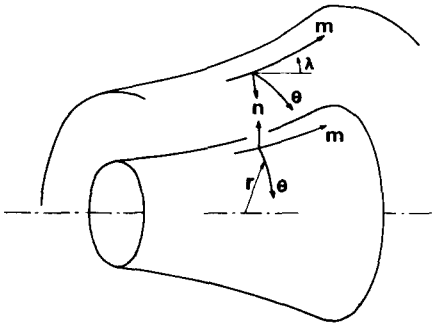

Figure 2 Coordinate system

$$+\frac{\sin\lambda}{R}(\theta_{\theta\theta}-\delta\tan^2\mu)=\frac{\tau_w\cos(\varepsilon_w+\mu)}{\rho C_m^2} \tag{1}$$

and the θ-momentum integral equation

$$\frac{d\theta_{\theta m}}{dm}-\tan\mu\frac{d}{dm}(\delta-\delta_m^*)+\left(2\frac{\sin\lambda}{R}+K_n+\frac{2}{C_m}\frac{dC_m}{dm}\right)\theta_{\theta m}$$

$$-\tan\mu\left(\frac{1}{C_m}\frac{dC_m}{dm}+\frac{\sin\lambda}{R}+K_n\right)(\delta-\delta_m^*)=-\frac{\tau_w\sin(\varepsilon_w+\mu)}{\rho C_m^2} \tag{2}$$

Here the displacement and momentum thicknesses are defined as follows:

$$\delta_m^*=\int_0^\delta\left(1-\frac{v_m}{C_m}\right)dn$$

$$\theta_{mm}=\int_0^\delta\left(1-\frac{v_m}{C_m}\right)\frac{v_m}{C_m}dn \tag{3}$$

$$\theta_{\theta\theta}=\int_0^\delta\left(\frac{v_\theta}{C_m}\right)^2dn$$

$$\theta_{\theta m}=\int_0^\delta\frac{v_m v_\theta}{C_m^2}dn$$

C_m and C_θ are the m- and θ-components of the mainstream flow velocity C_s at the edge of the boundary layer, and v_m and v_θ are the velocity components, in m and θ directions, within the boundary layer. The quantity $\mu=\arctan(C_\theta/C_m)$ is the angle between the streamlines at the edge of the boundary layer and the meridian plane, and K_n is the curvature, at the edge of the boundary layer, of the line orthogonal to the projections of the streamlines on the meridian plane (and along which the coordinate n is measured). From the definition of curvature,[15] it can be easily found that

$$K_n=\tan\lambda\frac{d\lambda}{dm}$$

since $(dr/dx)_m=\tan\lambda$, where λ is the angle of the m direction with the axis of symmetry (Figure 2). In the particular case of diffuser flows, $d\lambda/dm$ is generally small, and terms K_n in Equations 1 and 2 may be ignored. The wall shear stress τ_w makes an angle ε_w with the free-stream velocity and is positive if it opposes the main flow direction. It is worth noting that δ_m^* and θ_{mm} have the usual meanings of deficit of flow rate and momentum, while the same is not true for $\theta_{\theta m}$ and $\theta_{\theta\theta}$. In fact the latter, as are defined here, represent not a deficit but the

Notation

a_i, b_i, c_i, d_i, f_i	Coefficients in differential equations
c_f	$\tau_{w_s}/(\frac{1}{2}\rho C_s^2)$, friction coefficient
C_m, C_θ, C_n	Components of C_s in (m, θ, n) directions
C_s	Streamwise velocity at the edge of boundary layer
C_τ	$(\tau_w/\rho)^{1/2}$, friction velocity
E	Entrainment rate
G_i	Boundary-layer functions
H	δ_s^*/θ_{ss}, shape factor
k	0.40, constant of Coles' velocity profile
K_m, K_n	Curvature of the lines $n=$const., $m=$const., respectively
l	Diffuser length
(m, θ, n)	Coordinate system (Figure 2)
(r, θ, x)	Cylindrical coordinate system
r_c	Curvature radius of streamlines
R	Wall radius
R_{c_t}, R_{c_h}	Inviscid flow boundary radius at tip and hub, respectively
(s, p, z)	Coordinate system (Figure 1)
v_m, v_θ, v_n	Velocity components in (m, θ, n) coordinates
v_s, v_p, v_z	Velocity components in (s, p, z) coordinates
Greek symbols	
δ	Boundary-layer thickness
δ^*	Displacement thickness
ε	Arctan(v_p/v_s), angle between local flow direction and free-stream direction
ε_w	Angle between wall shear stress direction and free-stream direction
θ	Momentum thickness
λ	dr/dm (Figure 3)
Λ_s	δ_s^*/δ, shape parameter
μ	Arctan (C_θ/C_m), angle between the streamlines at the edge of the boundary layer and the meridian plane
ν	Kinematic viscosity
Π	Coles' wake parameter
ρ	Density
τ_w	Wall shear stress
ω	$(\tau_w/\rho C_s^2)^{1/2}$, dimensionless friction velocity

momentum in the θ direction. This explains why the wall shear stress terms have different signs in the two momentum equations.

The functions $\mu(m)$, $\lambda(m)$, $C_s(m)$, and $R(m)$ that characterize the external flow and the wall geometry can be considered as input to our boundary-layer calculation. In this case, the unknowns in Equations 1 and 2 are δ, τ_w, ε_w, and the four integral parameters.

To solve these equations, assumptions need to be made about the shape of the streamwise and secondary flow profiles, $v_s(z)$ and $v_p(z)$, in order that displacement and momentum thicknesses may be calculated. The Coles' velocity profile[16] was taken to describe the streamwise velocity:

$$\frac{v_s}{C_\tau}=\frac{1}{k}\ln\left(\frac{C_\tau z}{\nu}\right)+\frac{\Pi}{k}\left(1-\cos\frac{\pi z}{\delta}\right)+C \tag{4}$$

where $C_\tau=(\tau_w/\rho)^{1/2}$ is the friction velocity, Π is the Coles' wake factor, k and C are universal constants, ν represents the kinematic viscosity, and z is the coordinate perpendicular to the wall. This profile was checked with a variety of measured profiles in turbomachinery and was found to show a fairly good fitting to the experimental streamwise velocity profile.[8,17]

A variety of family profiles has been proposed to describe the cross-flow.[10] The Prandtl–Mager profile introduces only one extra parameter (the angle ε_w):

$$\frac{v_p}{v_s}=\tan\varepsilon=\tan\varepsilon_w\left(1-\frac{z}{\delta}\right)^2 \tag{5}$$

where ε is the local angle between the flow direction and the free-stream direction, and ε_w is the limiting value of ε when $z\to 0$, i.e., the angle between the free-stream direction and the wall shear stress (Figure 1). This parameter indicates the importance of the secondary flow in comparison with the main flow.[7]

The expressions of integral parameters (Equations 3) can now be derived by performing the integrations analytically. For each of these parameters, a solution is obtained in terms of δ, Π, ε_w, and the wall shear stress coefficient ω:

$$\omega=\left(\frac{\tau_{w_s}}{\rho C_s^2}\right)^{1/2}=\left(\frac{c_f}{2}\right)^{1/2} \tag{6}$$

These calculations were first performed in the orthogonal coordinate system (s, p, z) of Figure 1 with the axis s in the direction of the streamwise velocity. The parameters δ_s^*, δ_p^*, θ_{ss}, θ_{pp}, and θ_{ps} are defined as in the (m, θ, n) coordinate system (Appendix A). The results of the analytical integrations are

$$\begin{aligned}
\delta_s^* &= \omega\delta G_1\\
\theta_{ss} &= \omega\delta(G_1-\omega G_2)\\
\delta_p^* &= \delta\tan\varepsilon_w(1/3-\omega G_3)\\
\theta_{ps} &= \delta\tan\varepsilon_w(1/3-2\omega G_3+\omega^2 G_4)\\
\theta_{pp} &= \delta\tan^2\varepsilon_w(1/5-\omega G_5+\omega^2 G_6)
\end{aligned} \tag{7}$$

where $G_1, G_2, \ldots, G_6$ are functions of Π given in Appendix A.

We note that

$$\begin{aligned}
C_m &= C_s\cos\mu\\
v_m &= v_s\cos\mu - v_p\sin\mu\\
v_\theta &= v_s\sin\mu + v_p\cos\mu
\end{aligned}$$

and so we relate the integral parameters of Equations 3 in the coordinate system (m, θ, n) to the integral parameters of Equations 7 in the (s, p, z) coordinate system as follows:

$$\begin{aligned}
\delta_m^* &= \delta_s^*+\delta_p^*\tan\mu\\
\theta_{mm} &= \theta_{ss}+\tan\mu(2\theta_{ps}-\delta_p^*-\theta_{pp}\tan\mu)\\
\theta_{\theta\theta} &= (\delta-\delta_s^*-\theta_{ss})\tan^2\mu+\theta_{pp}+2\theta_{ps}\tan\mu\\
\theta_{\theta m} &= (\delta-\delta_s^*-\theta_{ss}-\theta_{pp})\tan\mu+\theta_{ps}(1-\tan^2\mu)
\end{aligned} \tag{8}$$

By introducing relationships 7 and 8, the momentum equations (Equations 1 and 2) may be expressed in the following form, in terms of δ, Π, ω, and ε_w (Appendix B):

$$a_i\frac{d\delta}{dm}+b_i\frac{d\Pi}{dm}+c_i\frac{d\omega}{dm}+d_i\frac{d\varepsilon_w}{dm}=f_i \qquad i=1,2 \tag{9}$$

Two additional equations are needed to solve Equation 9. The first one concerns the wall shear stress, which can be derived from Coles' profile taking $z=\delta$ in Equation 4:

$$\frac{1}{\omega}=\frac{1}{k}\ln\omega+\frac{1}{k}\ln\frac{C_s\delta}{\nu}+\frac{2\Pi}{k}+C \tag{10}$$

We recall that ω (Equation 6) represents the dimensionless wall shear stress component in the streamwise direction s (Figure 1).

To obtain the second equation, we will look for an empirical relationship describing the boundary-layer development. Following Le Balleur,[18,19] we combine the continuity equation and the local m momentum equation, for $n=\delta$, obtaining

$$\frac{d\delta}{dm}-\frac{C_n}{C_m}=\frac{1}{\rho C_m}\left[\frac{\partial\tau_{sn}/\partial n}{\partial v_s/\partial n}\right]_{n=\delta} \tag{11}$$

A similar expression can be obtained for 2-D boundary layers.[20] In fact, the left-hand side of Equation 11 is the entrainment rate E of a 2-D boundary layer on a flat plate:

$$E=\frac{1}{C_s}\frac{d}{dm}\int_0^\delta v_m\,dn \tag{12}$$

Equation 11 shows that the growth of 3-D boundary layers on an axisymmetric surface with variable radius is related to the turbulence properties at the boundary-layer edge through the streamwise velocity, C_s, and can be modeled as for 2-D boundary layers on a flat plate. Equation 12, together with one of the following equilibrium entrainment relationships, is the last equation of the present method.

Head[21] assumed that the dimensionless entrainment rate can be taken as a function of the shape parameter H_1 alone, $H_1=(\delta-\delta_s^*)/\theta_{ss}$, and found the following empirical relationship for the 2-D boundary layer on a flat plate:

$$E=0.0306(H_1-3.0)^{-0.653} \tag{13}$$

Escudier and Nicoll,[22] based on the concept of effective viscosity in the wake region of a boundary-layer velocity profile, recommend

$$E=\frac{0.15}{k}\omega\Pi \tag{14}$$

where ω and Π are parameters of the streamwise profile. Escudier and Nicoll[22] found that their relationship (Equation 14) provides a slightly better agreement with experimental results than Head's relation (Equation 13).

The entrainment rate will not be directly affected by the presence of the secondary flow. This does not contradict the principles of boundary-layer development, since the secondary flow vanishes at the interface with the external flow. The presence of the secondary flow is expressed in the momentum equations. Head's relationship has been used before in 3-D boundary layers[7] with $H_1=(\delta-\delta_m^*)/\theta_{mm}$.

Differentiating Equation 10 with respect to m and manipulating Equation 12, we obtain two more equations of the form of Equations 9. Expressions for coefficients a_i, b_i, c_i, d_i, f_i, with $i=1, 2, 3, 4$, are shown in Appendix B.

The four equations can be solved by the Runge–Kutta

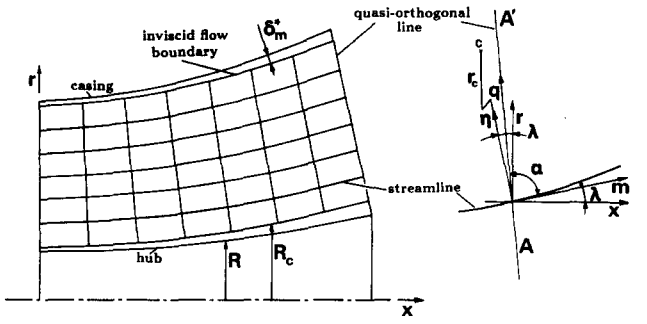

Figure 3 Streamlines of the meridian flow and geometry on a quasi-orthogonal line

method. The necessary initial values of the four variables are obtained from the boundary-layer integral parameters (Equations 7).

The inviscid method

The procedure used for the calculation of the axisymmetric swirling core flow was the streamline curvature method with quasi-orthogonal lines.[11–13] These are straight lines that join the inviscid flow boundaries and are roughly perpendicular to the streamlines projected on the meridian plane (Figure 3).

Assuming steady inviscid flow, without the presence of blade forces, the momentum equation can be written in the quasi-orthogonal direction q as follows:[12]

$$\frac{d}{dq}(1/2v_m^2)=\frac{dH}{dq}-T\frac{dS}{dq}-\frac{1}{2r^2}\frac{d}{dq}(r^2v_\theta^2)$$

$$-v_m^2K_m\sin\alpha+v_m\frac{\partial v_m}{\partial m}\cos\alpha \qquad (15)$$

where H represents the total enthalpy, T the static temperature, S the entropy, K_m the curvature of the meridional projection of the streamlines, and α the angle between the quasi-orthogonal line and the streamlines on the meridional plane (Figure 3).

Equation 15 for the variation of v_m along the quasi-orthogonal A–A' must be solved using a continuity equation in order that volume flow rate Q be conserved:

$$\int_A^{A'} 2\pi r v_m \sin\alpha\, dq = Q \qquad (16)$$

In duct inviscid flows, H, S, and the product rv_θ are conserved along streamlines. This allows the computation of the distributions of these quantities along the quasi-orthogonal lines. The last two terms in Equation 15 (the streamline curvature terms) are obtained iteratively.[12] Starting from an initial guess of the stream surface shapes, streamline curvature terms are computed by a simple parabolic fit through three points to obtain streamline shape and curvature. Equations 15 and 16 are then solved for each quasi-orthogonal line, giving the new v_m distribution and hence the new points of intersection of the stream surfaces with the quasi-orthogonal lines. A new streamline pattern is then obtained, allowing the calculation of the new values of streamline curvature and slope.

This method is valid for walls of revolution of arbitrary shape and imposes no limitations on the rotationality of the incoming flow.

Design of axisymmetric diffusers

The inviscid throughflow program computes the values of velocity and direction of the external flow needed for the boundary-layer calculation. An iterative procedure was used to displace the annular walls to account for the boundary-layer blockage effect. According to the present assumptions, the radius R_c of the inviscid core boundary is given by

$$R_c = R \pm \delta_m^*/\cos\lambda \qquad (17)$$

where the plus and minus signs refer to the hub and tip walls, respectively.

Having a calculation method for the entire flow, the question remains of what shape of diffuser walls will give the maximum static pressure recovery over a specified length. Kline and Strawn[2] propose a criterion for 2-D boundary layers based on the evolution of the shape parameter $\Lambda=\delta^*/\delta$. They suggested

$$\Lambda_p(m)=\Lambda_2-(\Lambda_2-\Lambda_1)\left[1-\left(\frac{m-m_1}{L}\right)^a\right] \qquad (18)$$

where subscripts 1 and 2 refer to the diffuser inlet and outlet cross sections, respectively, and showed that incipient detachment is obtained at the diffuser outlet with $\Lambda_2=0.42$ (the identical condition is proposed by Ahmed and Myring[6]). The exponent a defines the shape of the $\Lambda(m)$ curve. Typical values of a lie between 1 and 3.[2] According to this criterion, highest efficiencies are obtained for high values of a and Λ_2. The selection of high values of Λ_2 will lead to boundary-layer conditions close to detachment at the exit of the diffuser. Hence, if high values are chosen for both the exponent a and Λ_2, it follows that values of Λ_p close to Λ_2 will be obtained at sections far upstream from the diffuser exit. This is a dangerous design criterion, since it enhances the occurrence of stall if the real flow deviates slightly from the inlet design conditions.

Although the Kline and Strawn criterion has been proposed for 2-D boundary layers, it is possible to extend it to the evolution of $\Lambda_s=\delta_s^*/\delta$ in 3-D boundary layers if flow separation is not controlled essentially by the secondary flow. The adoption of this criterion is consistent with Coles' profile assumption for the external flow direction.

In the 3-D cases studied numerically by us, boundary-layer separation has been found for values of $\Lambda_s=0.25$ to 0.3 lower than those that characterize the separation in 2-D boundary layers. However, these values change with the geometry and the importance of the secondary flow. The limit value of Λ_2 to be adopted in the design calculations is chosen by studying the global behavior of the boundary-layer parameters.

The design procedure follows the algorithm shown in Figure 4. We start with a first guess of a stall-free geometry. Inviscid flow calculation gives hub and tip evolutions of the external velocity at the edge of boundary layer ($C_s(m)$ and $\mu(m)$). Boundary-layer calculation provides the new distributions of δ^* and Λ at the hub and tip walls. Equation 17 is then used to compute the inviscid core geometry. The following relationship between values of $\lambda(m)$ at iterations n and $n+1$ is used to correct diffuser geometry, in order to approximate the calculated and desired Λ^n and Λ_p evolutions:

$$\lambda^{n+1}(m)=\lambda^n(m)\left[1\mp\sigma_\lambda\left(1-\frac{\Lambda_p(m)}{\Lambda^n(m)}\right)\right] \qquad (19)$$

where σ_λ is a relaxation factor. To stabilize the iterative process, the shape of one of the walls is kept constant at each iteration. Finally, the diffuser length, L, is changed in order to achieve the required pressure recovery:

$$L^{n+1}=L^n\left[1-\sigma_L\left(1-\frac{\Delta\kappa_p}{\Delta\kappa^n}\right)\right] \qquad (20)$$

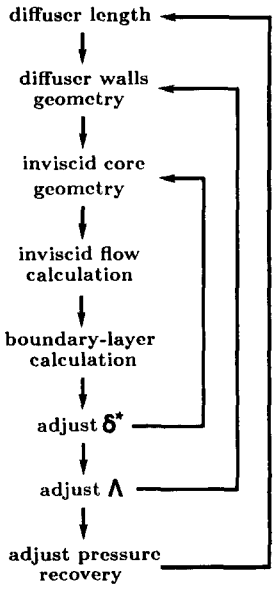

Figure 4 Flow chart for design procedure

where σ_L is the relaxation factor for the changes in the diffuser length, and $\Delta\kappa=\kappa_2-\kappa_1$ is the difference of the kinetic energy fluxes calculated along the inlet and outlet quasi-orthogonal lines,

$$\kappa=\rho\pi\int_{R_{c_t}}^{R_{c_h}}(v_m^2+v_\theta^2)v_m\sin\alpha r\,dq \tag{21}$$

We assume that the boundary layers are turbulent at the diffuser inlet, as is generally encountered in turbomachines. It is important to stress that the present method is particularly sensitive to the values of the inlet flow variables. The specification of inlet flow conditions will be based either on results of theoretical models for the flow upstream of the diffuser (if available) or on existing experimental data.

In general, the flow on one of the diffuser annular walls will be less favorable than on the other one, and so the prescribed $\Lambda_p(m)$ will not be met simultaneously at the two walls. The design method ensures that $\Lambda_p(m)$ is observed at the critical wall where the most adverse conditions take place.

Results

The boundary-layer method presented above was applied to two different test cases for which a sufficiently complete set of experimental data could be found in the literature. Figures 5 and 6 show the calculated results in comparison with experimental values and theoretical results from other authors. To assess the sensibility of the method, results from the relationships of both Head[21] and Escudier-Nicoll[22] are shown for the test cases.

Figure 5 shows the results of the method for the calculation of a 3-D boundary layer on a flat plate. This simulation is possible in our coordinate system, since the direction of the pressure gradient is constant and $\lambda=0$ (Equations 1 and 2). Detailed measurements are available for this flow.[23–25] Up to $x=0.5$ m, a good agreement is obtained between theoretical and experimental values for all boundary-layer parameters. Downstream of this section, 3-D separation occurs ($\mu+\varepsilon_w>90°$) for $\Lambda\approx0.25$, and the boundary-layer development is found to be appreciably underestimated by the method. This behavior is typical of the direct methods.[23–27] The theoretical calculation of Cousteix and Houdeville,[24] whose results are also shown in the same figure, was performed by an inverse method, prescribing δ_s^* and δ_p^* evolutions instead of velocity and direction of external flow.

The second test case is the 3-D boundary layer measured by Gardow[8] in a radial vaneless diffuser. Results of Figure 6 show

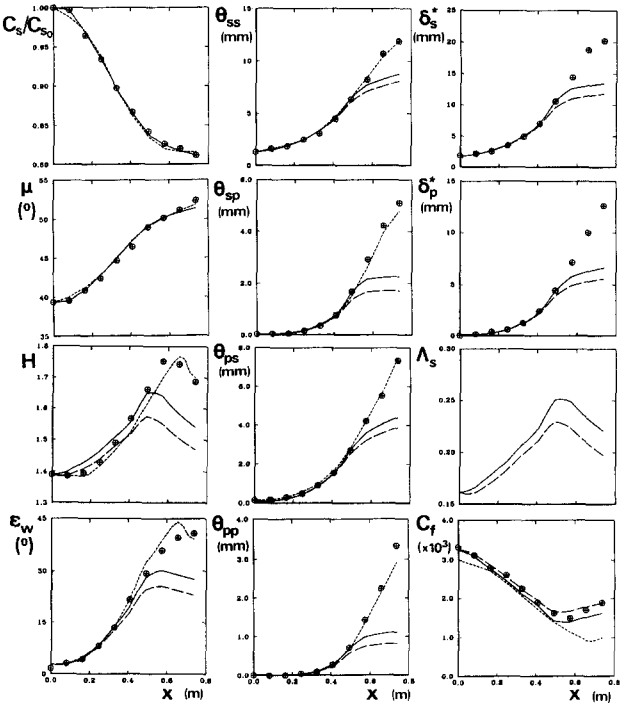

Figure 5 Three-dimensional boundary layer on a flat plate, under infinite swept-wing conditions. Comparisons between theoretical and measured values. ⊕, experiment. Calculation: ———, 3-D model with Head's equation; ———, the same, with Escudier-Nicoll relationship; – – – –, inverse method by Cousteix and Houdeville. Three-dimensional separation ($\mu+\varepsilon_w=90°$) occurs at $x=0.6$ m

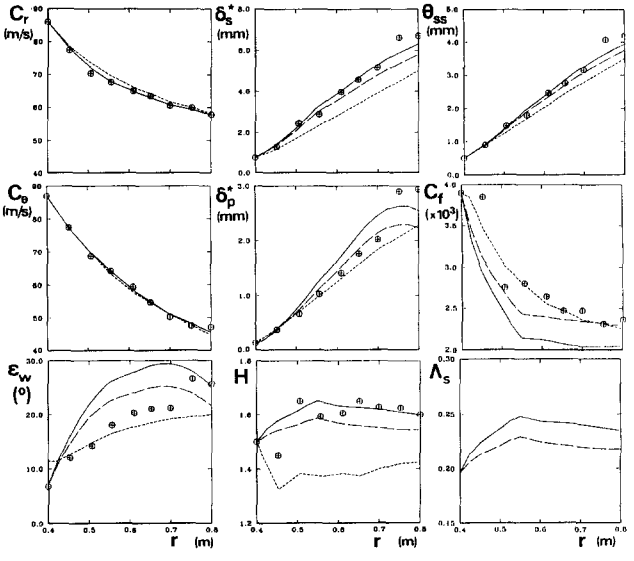

Figure 6 Three-dimensional boundary layer in a radial diffuser. Comparison between theoretical and measured values. ⊕, experiment. Calculation: ———, 3-D model with Head's equation; ———, the same, with Escudier-Nicoll relationship; – – – –, Ruyck-Hirsch model

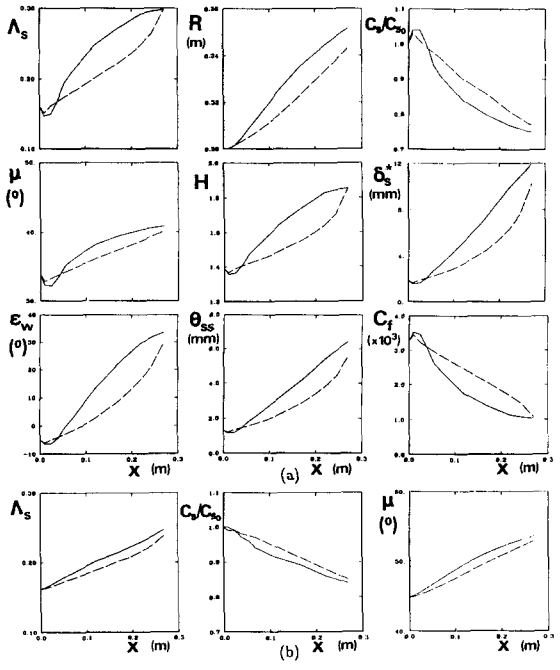

Figure 7 Design example for an axisymmetric annular diffuser. The inner wall shape and the diffuser length were given. The outer wall shape is shown for two different prescribed evolutions of $\Lambda_s = \delta_s^*/\delta$: ———, $a=2$; — — —, $a=0.6$. (a) Outer wall; (b) inner wall.

a fair agreement with experimental results, except for the C_f evolution, which has been underestimated by theory, and the ε_w evolution, which shows a less satisfactory agreement. Also shown in the same figure are the theoretical results of Ruyck and Hirsch[8] for the same example.

We note that the comparison of the results plotted in Figures 5 and 6 does not show clearly which of the two empirical relationships (Head's or Escudier-Nicoll's; see Equations 13 and 14) is more adequate for general use in our method. In fact, better agreement with experimental results is shown in Figure 5 when Escudier-Nicoll's relationship is used, whereas Figure 6 indicates the opposite.

Figure 7 shows the results of the application of the method described above to the design of an axisymmetric annular diffuser. As an example, free-vortex swirling flow was considered. Inlet flow conditions are shown in Table 1. A cylindrical inner wall was assumed and the diffuser length l was taken such that $l/h=2.7$, where h is the difference between the inner and outer wall radii at the inlet cross section. Eleven meridional streamlines and twelve quasi-orthogonal lines were considered for the inviscid core flow calculation. Two different evolutions of $\Lambda_p(m)$ (Equation 18) were considered: the first one, with $a=2$, corresponds to a strong pressure gradient at the beginning of the diffuser, where the boundary layer is in its healthiest condition; the second one, with $a=0.6$, has a larger pressure gradient at the end of the diffuser. In both evolutions, $\Lambda_2=0.3$ was adopted. About 20 iterations to correct diffuser geometry and 80 seconds CPU time on a VAX 6000-440 were needed to run these examples.

Results show that diffuser design can be performed based on Λ_p evolution. As expected, in each of the tested cases, the development of the boundary-layer parameter Λ follows in a qualitative way the prescribed evolution of the shape parameter Λ_p. An identical pressure recovery was obtained in both designs: about 50% of the kinetic energy associated with axial velocity component. This indicates that in Equation 18, the choice of the value of Λ_2 is more important than the choice of the value of the exponent a in giving the shape of the $\Lambda_p(m)$ curve. We recall that the calculated geometries of the outer wall, shown in Figure 7, are not substantially different from the conical shape, which is easy to manufacture.

Table 1 Inlet flow conditions for the design example

	Inner wall	Outer wall
R [m]	0.2	0.3
C_θ [m/s]	30	20
C_m [m/s]	30	30
δ [mm]	11.4	11.4
Π	0.6	0.6
ω	0.04	0.04
ε_w [°]	−5	−5

Conclusions

A theoretical model for turbulent incompressible 3-D boundary layers in axisymmetric ducts has been developed. The comparison between theoretical and experimental values shows a fair agreement for a variety of flows and geometries of practical interest in turbomachinery. A streamline curvature throughflow program was combined with the boundary-layer calculation method to predict swirling flows in annular ducts. The method proved to be suitable for diffuser design, since it allows a full control over boundary-layer development, although direct viscous coupling limit its use to attached boundary layers. In the design, inlet flow variables must be prescribed accurately.

Acknowledgment

The authors wish to thank Prof. A. F. de O. Falcão for his encouragement and advice. The work was partly supported by CTAMFUTL/INIC.

References

1 Stratford, B. S. An experimental flow with zero skin friction throughout its region of pressure rise. *J. Fluid Mech.*, 1959, **5**, 17–35

2 Strawn, R. C. and Kline, S. J. A stall margin design method for planar and axisymmetric diffusers. *ASME J. Fluids Eng.*, 1983, **105**, 28–33

3 Wilson, D. G. *The Design of High-Efficiency Turbomachinery and Gas Turbines.* MIT Press, Cambridge, MA, 1984

4 Voorde, C. B. van den and Bos, J. Measured and calculated turbulent boundary layer flow in a vaneless radial diffuser. *AGARD-AG-164* (J. Surugue, Ed.), 1972, 293–310

5 Bardina, J., Lyrio, A., Kline, S. J., Ferziger, J. H., and Johnston, J. P. A prediction method for planar diffuser flows. *ASME J. Fluids Eng.*, 1981, **103**, 315–321

6 Ahmed, N. M. A. and Myring, D. F. An inverse method for the design of axisymmetric optimal diffusers. *Int. J. Num. Meth. Eng.*, 1986, **22**, 377–394

7 Horlock, J. H. and Perkins, H. J. Annulus wall boundary layers in turbomachines. *AGARD-AG-185*, 1974, 1–60

8 Ruyck, J., Hirsch, C., and Kool, P. An axial compressor end-wall boundary layer calculation method. *ASME J. Eng. Power*, 1979, **101**(2), 233–249

9 Ruyck, J. and Hirsch, C. End-wall boundary layer calculations in multistage axial compressors. *AGARD-CP-351*, 1983, 19-1–19-16

10 Gostelow, J. P. *Cascade Aerodynamics*, Pergamon Press, Oxford, 1984

11 Novak, R. A. Streamline curvature computing procedures for fluid-flow problems. *ASME J. Eng. Power*, 1967, **89**(4), 478–490

12 Denton, J. D. Throughflow calculations for transonic axial flow turbines. *ASME J. Eng. Power*, 1978, **100**(2), 212–218

13 Gato, L. M. C. and Falcão, A. F. de O. Aerodynamics of the Wells turbine. *Int. J. Mech. Sci.*, 1988, **30**, 383–395

14 Morgado, F. T. F. and Gato, L. M. C. An integral calculation method for three-dimensional boundary-layers in axisymmetric diffusers. DER/LNETI Internal Report 25/88 (in Portuguese), Lisbon, 1988

15 Smirnov, V. I. *A Course of Higher Mathematics*, Vol. 1, Pergamon Press, Oxford, 1964

16 Coles, D. E. The law of the wake in the turbulent boundary layer. *J. Fluid Mech.*, 1956, **1**, 191–226

17 Sumner, W. J. and Shanebrook, J. R. Entrainment theory for compressible turbulent boundary layers on adiabatic walls. *AIAA J.*, 1971, **9**(2), 330–332

18 Le Balleur, J. C. Viscous-inviscid interaction and computation in aerodynamics. *Proc. BAIL V Conf.* (G. B. Yu and J. H. Miller, Eds.), Boole Press, Dublin, 1988, 1–12

19 Le Balleur, J. C. New possibilities of viscous-inviscid numerical techniques for solving viscous flow equations with massive separation. *Proceedings of the Fourth Symposium on Numerical and Physical Aspects of Aerodynamic Flows* (T. Cebeci, Ed.), Springer-Verlag, Berlin, 1990, 1–20

20 Michel, R., Quémard, C., and Durant, R. Application d'un schéma de longeur de mélange a l'étude des couches limites turbulentes d'équilibre. Note Technique no. 154, ONERA, Chatillon, 1969

21 Head, M. R. and Patel, V. C. Improved entrainment method for calculating turbulent boundary-layer development. ARC R&M 3643, 1969, 1–23

22 Escudier, M. P. and Nicoll, W. B. The entrainment function in turbulent boundary-layer and wall-jet calculations. *J. Fluid Mech.*, 1966, **25**, 337–366

23 Berg, B. van den, Elsenaar, A., Lindhout, J. P. F., and Wesseling, P. Measurements in an incompressible three-dimensional turbulent boundary layer, under infinite swept-wing conditions, and comparison with theory. *J. Fluid Mech.*, 1975, **70**(1), 127–148

24 Cousteix, J. and Houdeville, R. Singularities in three-dimensional turbulent boundary-layer calculations and separation phenomena. *AIAA J.*, 1981, **19**(8), 976–985

25 Cousteix, J. Three-dimensional boundary layers. Introduction to calculation methods. *AGARD-R-741*, 1987, 1-1–1-49

26 Smith, P. D. Direct and inverse integral calculation methods for three-dimensional turbulent boundary layers. *Aeronautical J.*, 1984, **88**, 155–159

27 Stock, H. W. Computation of the boundary layer and separation lines on inclined ellipsoids and of separated flows on infinite swept wings. AIAA 13th Fluid and Plasma Dynamics Conference, Colorado, AIAA Paper 80-1442, 1980

28 Abramowitz, M. and Stegun, A. *Handbook of Mathematical Functions*, Dover, New York, 1972

Appendix A

In the (s, p, z) coordinate system, the boundary-layer integral parameters are defined as

$$\delta_s^* = \int_0^\delta \left(1-\frac{v_s}{C_s}\right) dz$$

$$\theta_{ss} = \int_0^\delta \left(1-\frac{v_s}{C_s}\right)\frac{v_s}{C_s}\, dz$$

$$\delta_p^* = \int_0^\delta \frac{v_p}{C_s}\, dz \qquad \text{(A.1)}$$

$$\theta_{pp} = \int_0^\delta \left(\frac{v_p}{C_s}\right)^2 dz$$

$$\theta_{sp} = \int_0^\delta \left(1-\frac{v_s}{C_s}\right)\frac{v_p}{C_s}\, dz$$

$$\theta_{ps} = \int_0^\delta \frac{v_p v_s}{C_s^2}\, dz$$

We assume Coles' profile in the streamwise direction s (Equation 4, with $k=0.40$) and the Prandtl–Mager profile (Equation 5) in the normal direction. Performing the integrations above (Equations A.1) we obtain Equations 7, where

$$G_1 = \frac{1+\Pi}{k}$$

$$G_2 = \frac{1}{k^2}\left[2+\left(2+2\frac{Si(\pi)}{\pi}\right)\Pi+\frac{3}{2}\Pi^2\right]$$

$$= \frac{1}{k^2}(2+3.1787\Pi+1.5\Pi^2)$$

$$G_3 = \frac{1}{k}\left[\frac{11}{18}+\left(\frac{1}{3}+\frac{2}{\pi^2}\right)\Pi\right]$$

$$= \frac{1}{k}(0.6111+0.5360\Pi)$$

$$G_4 = \frac{1}{k^2}\left\{\frac{85}{54}+\left[\frac{11}{9}+\frac{2}{\pi^2}\left(\pi Si(\pi)+2\ln\pi-3+2\gamma\right.\right.\right.$$

$$\left.\left.\left.-2Ci(\pi)-\frac{2}{\pi}Si(\pi)\right)\right]\Pi+\left(\frac{1}{2}+\frac{17}{4}\frac{1}{\pi^2}\right)\Pi^2\right\}$$

$$= \frac{1}{k^2}(1.5741+2.2221\Pi+0.9306\Pi^2)$$

$$G_5 = \frac{1}{k}\left[\frac{137}{150}+\left(\frac{2}{5}+\frac{8}{\pi^2}-\frac{48}{\pi^4}\right)\Pi\right] = \frac{1}{k}(0.9133+0.7178\Pi)$$

$$G_6 = \frac{1}{k^2}\left\{\frac{12019}{9000}+\left[\frac{137}{150}+\frac{2}{\pi^2}\left(\pi Si(\pi)+4\ln\pi-\frac{12}{\pi}Si(\pi)\right.\right.\right.$$

$$\left.\left.-5+4\gamma-4Ci(\pi)-\frac{26}{\pi^2}+\frac{24}{\pi^3}Si(\pi)\right)+\frac{8}{\pi^4}\left(22-6\ln\pi\right.\right.$$

$$\left.\left.\left.+6Ci(\pi)-6\gamma\right)\right]\Pi+\left(\frac{3}{10}+\frac{17}{2}\frac{1}{\pi^2}-\frac{195}{4}\frac{1}{\pi^4}\right)\Pi^2\right\}$$

$$= \frac{1}{k^2}(1.3354+1.7329\Pi+0.6608\Pi^2)$$

The functions $S_i(z)$ and $C_i(z)$ are the sine and cosine integral,[28] and $\gamma=0.5772\ldots$ is the Euler constant.[28] With $G_i' = \partial G_i/\partial\Pi$, we obtain

$$G_1' = 1/k$$

$$G_2' = (3.1787+3.0\Pi)/k^2$$

$$G_3' = 0.5360/k$$

$$G_4' = (2.2221+1.8612\Pi)/k^2$$

$$G_5' = 0.7178/k$$

$$G_6' = (1.3729+1.3216\Pi)/k^2$$

Appendix B

Equations 7 and 8 are used to derive expressions for the coefficients a_i, b_i, c_i, d_i, f_i, with $i=1, 2, 3, 4$, of the system of four equations solved in the boundary-layer method. The results are

$$a_1 = \omega(G_1-\omega G_2)+\tan\mu\tan\varepsilon_w(1/3-3\omega G_3+2\omega^2 G_4)$$
$$-\tan^2\mu\tan^2\varepsilon_w(1/5-\omega G_5+\omega^2 G_6)$$

$$b_1=\omega\delta[(G_1'-\omega G_2')+\tan\mu\tan\varepsilon_w(-3G_3'+2\omega G_4')$$
$$+\tan^2\mu\tan^2\varepsilon_w(G_5'-\omega G_6')]$$
$$c_1=\delta[(G_1-2\omega G_2)+\tan\mu\tan\varepsilon_w(-G_3+2\omega G_4)$$
$$-\tan^2\mu\tan^2\varepsilon_w(G_5-2\omega G_6)]$$
$$d_1=\delta\tan\mu\sec^2\varepsilon_w[(1/3-3\omega G_3+2\omega^2 G_4)$$
$$+\tan\mu\tan\varepsilon_w(-1/5+\omega G_5-\omega^2 G_6)]$$
$$f_1=-\frac{1}{C_m}\frac{\partial C_m}{\partial m}(2\theta_{mm}+\delta_m^*)-\left(\frac{\sin\lambda}{R}+K_n\right)\theta_{mm}$$
$$-\frac{\sin\lambda}{R}(\theta_{\theta\theta}-\delta\tan^2\mu)+\omega^2\frac{\cos(\varepsilon_w+\mu)}{\cos^2\mu\cos\varepsilon_w}$$
$$-\sec^2\mu\frac{d\mu}{dm}(2\theta_{ps}-2\theta_{pp}\tan\mu-\delta_p^*)$$
$$a_2=-\tan\mu[a_4-1+\omega(2G_1-\omega G_2)+\tan^2\varepsilon_w(1/5-\omega G_5$$
$$+\omega^2 G_6)]+(1-\tan^2\mu)\tan\varepsilon_w(1/3-2\omega G_3+\omega^2 G_4)$$
$$b_2=-\omega\delta\{\tan\mu[2G_1'-\omega G_2'-\tan^2\varepsilon_w(G_5'-\omega G_6')]$$
$$+(1-\tan^2\mu)\tan\varepsilon_w(2G_3'-\omega G_4')\}-b_4\tan\mu$$
$$c_2=-\tan\mu[c_4+\delta(2G_1-2\omega G_2)-\delta\tan^2\varepsilon_w(G_5-2\omega G_6)]$$
$$-2\delta(1-\tan^2\mu)\tan\varepsilon_w(G_3-\omega G_4)$$
$$d_2=\delta\sec^2\varepsilon_w[2\tan\varepsilon_w(1/5-\omega G_5+\omega^2 G_6)$$
$$+(1-\tan^2\mu)(1/3-2\omega G_3+\omega^2 G_4)]-d_4\tan\mu$$
$$f_2=-\left(\frac{2}{C_m}\frac{dC_m}{dm}+K_n+2\frac{\sin\lambda}{R}\right)\theta_{\theta m}-\omega^2\frac{\sin(\varepsilon_w+\mu)}{\cos^2\mu\cos\varepsilon_w}$$
$$+\tan\mu\left(\frac{1}{C_m}\frac{dC_m}{dm}+K_n+\frac{\sin\lambda}{R}\right)(\delta-\delta_m^*)$$
$$-\sec^2\mu\frac{d\mu}{dm}(\delta-\delta_s^*-\theta_{ss}-\theta_{pp}-2\theta_{ps}\tan\mu+\delta_p^*\tan\mu)$$
$$a_3=1/\delta$$
$$b_3=2$$
$$c_3=1/\omega+k/\omega^2$$
$$d_3=0$$
$$f_3=-\frac{1}{C_s}\frac{dC_s}{dm}$$
$$a_4=1-\omega G_1-\tan\mu\tan\varepsilon_w(1/3-\omega G_3)$$
$$b_4=-\omega\delta(G_1'-\tan\mu\tan\varepsilon_w G_3')$$
$$c_4=-\delta(G_1-\tan\mu\tan\varepsilon_w G_3)$$
$$d_4=-\delta\tan\mu\sec^2\varepsilon_w(1/3-\omega G_3)$$
$$f_4=E\sec\mu-\frac{1}{C_m}\frac{dC_m}{dm}(\delta-\delta_m^*)+\sec^2\mu\frac{d\mu}{dm}\delta_p^*$$